1-1-2018

Ultrathin and Edge-Enriched Holey Nitride Nanosheets as Bifunctional Electrocatalysts for the Oxygen and Hydrogen Evolution Reactions

Haipeng Guo
University of Wollongong, hg476@uowmail.edu.au

Boyang Ruan
University of Wollongong, boyang@uow.edu.au

Wenbin Luo
University of Wollongong, luow@uow.edu.au

Jianqiu Deng
Laboratory of Information Materials, Guilin University of Electronic Technology, jianqiu@uow.edu.au

Jiazhao Wang
University of Wollongong, jiazhao@uow.edu.au

See next page for additional authors

Ultrathin and Edge-Enriched Holey Nitride Nanosheets as Bifunctional Electrocatalysts for the Oxygen and Hydrogen Evolution Reactions

Abstract

Exploring economically efficient electrocatalysts with good electrocatalytic activity is essential for diverse electrochemical energy devices. Series of ultrathin metallic nickel-based holey nitride nanosheets were designed as bifunctional catalysts for the oxygen evolution reaction (OER) and hydrogen evolution reaction (HER). They exhibit improved catalytic properties owing to the inherent advantages of their plentiful active reaction sites resulting from the complete exposure of the atoms in the large lateral surfaces and from the edges of pore areas, together with expanded lattice spacing distance. This obtained three-dimensional conductive integral architecture can not only accelerate the electron transportation by the highly orientated crystalline structure but also facilitate the diffusion of intermediate and gases. In terms of the OER electrocatalytic properties, a quite low overpotential (300 mV) is required for the holey two-dimensional (2D) Ni3Fe nitride nanosheets to deliver a current density of about 100 A g-1, with an enhanced improvement over IrO2by a factor of nearly 25 times. The holey 2D Ni3Fe nitride nanosheets also exhibit enhanced catalytic performance toward the HER, with a tiny overpotential (233 mV) to achieve a current density of about 100 A g-1with much better kinetic properties in comparison to those of highly active Pt/C.

Disciplines

Engineering | Physical Sciences and Mathematics

Publication Details

Guo, H., Ruan, B., Luo, W., Deng, J., Wang, J., Liu, H. & Dou, S. (2018). Ultrathin and Edge-Enriched Holey Nitride Nanosheets as Bifunctional Electrocatalysts for the Oxygen and Hydrogen Evolution Reactions. ACS Catalysis, 8 (10), 9686-9696.

Authors

Haipeng Guo, Boyang Ruan, Wenbin Luo, Jianqiu Deng, Jiazhao Wang, Hua-Kun Liu, and Shi Xue Dou

Ultrathin and Edge-Enriched Holey Nitride Nanosheets as Bifunctional Electrocatalysts for the Oxygen and Hydrogen Evolution Reactions

Hai-Peng Guo[†], Bo-Yang Ruan[†], Wen-Bin Luo[†], Jianqiu Deng[‡], Jia-Zhao Wang*[†], Hua-Kun Liu[†], Shi-Xue Dou[†]*

[†] Institute for Superconducting and Electronic Materials, University of Wollongong, Squires Way, Fairy Meadow, NSW 2500, Australia

[‡] School of Material Science and Engineering & Guangxi Key Laboratory of Information Materials, Guilin University of Electronic Technology, Guangxi, Guilin 541004, China

ABSTRACT: Exploring economically efficient electrocatalysts with good electrocatalytic activity is essential for diverse electrochemical energy devices. Series of ultrathin metallic nickel-based holey nitride nanosheets were designed as bifunctional catalysts for the oxygen evolution reaction (OER) and hydrogen evolution reaction (HER). They exhibit improved catalytic properties owing to the inherent advantages of their plentiful active reaction sites resulting from the complete exposure of the atoms in the large lateral surfaces and from the edges of pore areas, together with expanded lattice spacing distance. This obtained three-dimensional conductive integral

architecture can not only accelerate the electron transportation by the highly orientated crystalline structure, but also facilitate the diffusion of intermediate and gases. In terms of the OER electrocatalytic property, a quite low overpotential (300 mV) is required for the holey two-dimensional (2D) Ni_3Fe nitride nanosheets to deliver a current density about 100 A g^{-1}, with an enhanced improvement than IrO_2 by a factor of nearly 25 times. The holey 2D Ni_3Fe nitride nanosheets also exhibit enhanced catalytic performance towards the HER, with a tiny overpotential (233 mV) to achieve the current density about 100 A g^{-1} and much better kinetic property than those of highly-active Pt/C.

Keywords: Two-dimensional; Nitride electrocatalyst; LDH; Oxygen evolution reaction; Hydrogen evolution reaction

1. INTRODUCTION

Ultrathin two-dimensional (2D) holey nanostructures have drawn significant research attention for energy storage, catalysis, electronics, and biomedical science because their unique feature could provide unprecedented chemical, electronic, and physical properties resulting from the electron confinement in two dimensions. [1-6] Due to their huge lateral surface area and atomic thickness, this special feature allows for direct correlation between the properties and the structure, giving superior atomic transport. They are frequently used as a bridge between microscale and nanoscale features to realize the fabrication of future microscale devices. [7-11] In contrast to the intact lateral surface, the holes on the lateral surface will result in ultrahigh specific surface area and a continuously connected integrated network, while maintaining atomic thickness, because the reaction intermediates can easily be transferred and diffuse throughout the whole porous system, not only along the large lateral surface direction, but also through holes on the surface, which can be considered as channels among numerous nanosheets. [12-18] 2D holey nanosheets have inherent

advantages for surface-related applications such as catalysis. For example, owing to the complete exposure of the large lateral surface atoms and the much greater number of catalytic active atoms in the hole area, it will dramatically accelerate the reaction kinetics, which would be much more favorable for achieving outstanding electrocatalytic performance towards the oxygen evolution reaction (OER) and hydrogen evolution reaction (HER). [8, 19] Meanwhile, this ultrathin holey 2D structure also presents excellent properties through accelerating the diffusion of the evaluated gases and electrolyte accessibility. [2, 20] Moreover, because of the excellent mechanical strength from the strong in-plane covalent bonds, this 2D porous nanostructured catalyst can also alleviate or even solve many of physical issues regarding state-of-the-art nanoparticle catalysts, such as aggregation or peeling off during the reaction, resulting in significant descent of the electrocatalytic performance. [7, 21-26] A number of 2D structured materials are employed as catalysts to facilitate the sluggish evolution reaction kinetics, for example precious metals, metal hydroxides/oxides, and metal sulfides. [22, 27-38] Among these, transition metal nitrides have the inherent advantages of high catalytic activity, economic efficiency, and superior electrical conductivity due to the introduction of nitrogen atoms into the metal hosts, which exhibit a metallic state with continuous conductivity near the Fermi level according to the computer calculations. [32, 39-43] Therefore, in this work, a strategy is proposed to develop ultrathin 2D holey structured bimetallic nitride materials with a strong high-orientation crystalline texture. A series of ultrathin 2D holey nickel-based nitrides (Ni_3M nitride, M = Fe, Co, Mn) has been designed and successfully synthesized, with a satisfactory specific surface area (189.6 m^2 g^{-1}), maintaining 0.6 - 0.8 nm nanosheet thickness. The hierarchical porous continuously conductive architecture caused by the holey nitride nanosheets is much more beneficial to transport of reaction intermediates and gas diffusion throughout the entire electrode. The faster electron transportation along the ultrathin 2D

direction can be further enhanced by their nearly single-crystalline structure, while the superior electrocatalytic performance could be ascribed to the highly exposed atoms on the large lateral surfaces, resulting from the vast surface area and plentiful exposed catalytically active atoms or lattice planes in the hole area. Furthermore, the influence of lattice spacing on the catalytic activities was investigated by comparing three different nickel-based nitrides which have different lattice spacing after introducing nitrogen.

2. EXPERIMENTAL SECTION

Synthesis of Ni_3Fe-LDH. The Ni_3Fe-LDH nanosheets were synthesized based on previous procedures. [44] In general, $Fe(NO_3)_3 \cdot 9H_2O$ (140 mg) and $NiCl_2$ (188 mg) were dispersed into deionized (DI) water (80 mL) under severely stirring for 10 min, followed by adding urea (168 mg) and $Na_3C_6H_5O_7$ (5.16 mg). After another 10 min, the reaction proceeded for 24 h with a Teflon-lined autoclave under 150 ˚C. The Ni_3Fe-LDH was obtained after washing three times by ethanol and DI water.

Synthesis of Ni_3Co-LDH. The Ni_3Co-LDH nanosheets were fabricated based on previous procedures. [45] In general, $Ni(NO_3)_2 \cdot 6H_2O$ (727 mg), $CO(NH_2)_2$ (2.25 g), and $Co(NO_3)_2 \cdot 6H_2O$ (1153 mg) were dispersed into DI water to form a mixture (50 mL) with a volume ratio of $V_{(\text{ethylene glycol})}/V_{(\text{DI water})} = 3{:}1$. After refluxing 3 h under 90 ˚C, the product was collected after washing three times by ethanol and DI water.

Synthesis of Ni_3Mn-LDH. The Ni_3Mn-LDH nanosheets were synthesized with previous procedures. [46] In general, $Ni(NO_3)_2 \cdot 6H_2O$ (245 mg), $NaNO_3$ (153 mg), NH_4F (185 mg), and

$Mn(NO_3)_2 \cdot 4H_2O$ (50 mg) were added into DI water (250 mL) under severely stirring with N_2 atmosphere. After 30 min, H_2O_2 (30 wt. %, 25 μL) was added dropwise into the solution. NaOH solution (50 mL, 0.12 M) was then dispersed dropwise into the solution. After stirring 12 h under room temperature, the product was collected after washing three times by ethanol and DI water.

Synthesis of holey 2D nitride nanosheets. To synthesize holey 2D Ni_3Fe nitride, Ni_3Co nitride, and Ni_3Mn nitride nanosheets, Ni_3Fe LDH, Ni_3Co LDH, and Ni_3Mn LDH nanosheets were calcined 1 min at NH_3 atmosphere at 500 ˚C (ramp rate about 10 ℃ min^{-1}).

Materials characterizations. The crystalline structures were analyzed with GBC MMA powder X-ray diffraction. As for the morphologies, JEOL JSM-7500FA scanning electron microscopy and JEM-ARM200F transmission electron microscopy were utilized. Atomic force microscopy was from Asylum AFM facility. The specific surface areas were investigated through Quantachrome Instruments Autosorb iQ2 through N_2 adsorption at -196 °C with Brunauer-Emmett-Teller (BET) method. The vacuum pressure was kept under 10^{-4} Pa to degas the samples at 100 °C. The mean value was calculated after obtaining three measurements for each sample. The conductivities of the samples were measured by the four-probe method (9 T Physical Properties Measurement System).

Electrochemical measurements: A three-electrode glasscell with an Ag/AgCl reference electrode and a graphite rod counter electrode on Princeton 2273 and 616 workstations were employed to test electrochemical performance. [47] In order to make the catalyst inks, sample (5 mg) was added in mixed solution (1100 μL) with 5 % Nafion® solution (100 μL), isopropanol (250 μL), and DI water (750 μL). The working electrodes were obtained through dripping the catalyst

ink (5 μL) on the pre-polished glassy carbon disk electrodes and drying for 20 min at 80 °C oven. Linear sweep voltammetry were performed use 1 M KOH. Electrochemical impedance spectroscopy tests were conducted at 0.607 V. To determine the active surface areas, electrochemical double-layer capacitance measurements was performed between 0.2 and 0.3 V at various scan rates. All potentials were referenced to reversible hydrogen electrode (RHE) with the following calculation: E_{RHE} = 0.059 pH + 0.197 + $E_{Ag/AgCl}$. For the overall water-splitting performance, nickel foam (1 cm^2) was utilized as working electrode. And the active material loading was 0.3 mg cm^{-2}. SRI 8610C gas chromatograph was utilized to record the evaluated H_2 gas during the overall water splitting. Faradaic efficiency is calculated with the following equation:

$$\text{Faradaic efficiency} = \frac{V/Vm}{Q/(2*\mathrm{F})}$$

where V is the volume of H_2 gas experimentally evolved, V_m is the molar volume (24.5 L mol^{-1}), Q stands for the number of charge travelled through two electrodes, 2 means 2 moles of electrons per mole for H_2, and F represents the Faraday constant (96485 C mol^{-1}).

Calculation Method: The Vienna Ab-initio Simulation Package package was utilized when carring out the density functional theory for the First-principle calculations. In order to define electronic exchange and correlation effects, the generalized gradient approximation with the Perdew-Burke-Ernzerhof functional was employed. For geometric optimization, Methfessel-Paxton electronic smearing and uniform G-centered k-points meshes (resolution of 2π*0.035 $Å^{-1}$) were employed for the Brillouin zone integration. One cutoff energy (550 eV) was applied during the computations. Above parameters guarantee that the total energies convergence is below 1 meV/atom. After relax of the structure, forces between atoms were below 1 meV $Å^{-1}$ with the complete stress tensor less than 0.01 GPa of the target number.

3. RESEARCH AND DISCUSSION

The synthesis strategy for the ultrathin 2D holey nitride materials is illustrated in **Figure 1(a)**. The morphology and structure are characterized with scanning electron microscopy (SEM) and X-ray diffraction (XRD). A series of nickel-based layered double hydroxide (LDH) nanosheets were synthesized as precursors, including Ni_3Fe LDH, Ni_3Co LDH, and Ni_3Mn LDH, as illustrated in transmission electron microscopy (TEM) images (**Figure 2a, d, g)**. All the LDH samples showed a uniform, silk-like, 2D nanosheet structure with big lateral size about several micrometers. In the following nitridation by annealing in an NH_3 atmosphere, the corresponding nitride products were obtained with numerous holes on the in-plane surface, as revealed in Figure 1(b, c, d) and Figure 2(b, e, h), but the products still maintained the 2D nanosheet structure. All the nitride materials exhibit a standard cubic diffraction pattern corresponding to (111), (200), and (220) planes as shown in Figure 1(e, f). [32-33, 40] The distances of corresponding lattice spacing of Ni_3Fe nitride is much larger than those of Ni_3Co nitride and Ni_3Mn nitride, which could modify the distance of surface atoms with varying the surface electronic structure and catalytic activity.[48-49] As can be seen from **Figure S1**, compared with metallic state samples, the peaks of three samples have been shifted to the left after introducing nitrogen, indicating that the nitrogen could increase the lattice spacing of the metallic state materials. The peak shifts of Ni_3Fe is much larger than the Ni_3Co and Ni_3Mn as well, implying that the lattice spacing of Ni_3Fe nitride is significantly increased after the induction of nitrogen. The morphology of the nitride materials is much more uniform than that of the oxide materials, indicating that the nitrogen also could assist the form of uniform nanopores on the nanosheets, as can be seen from **Figure S2**.

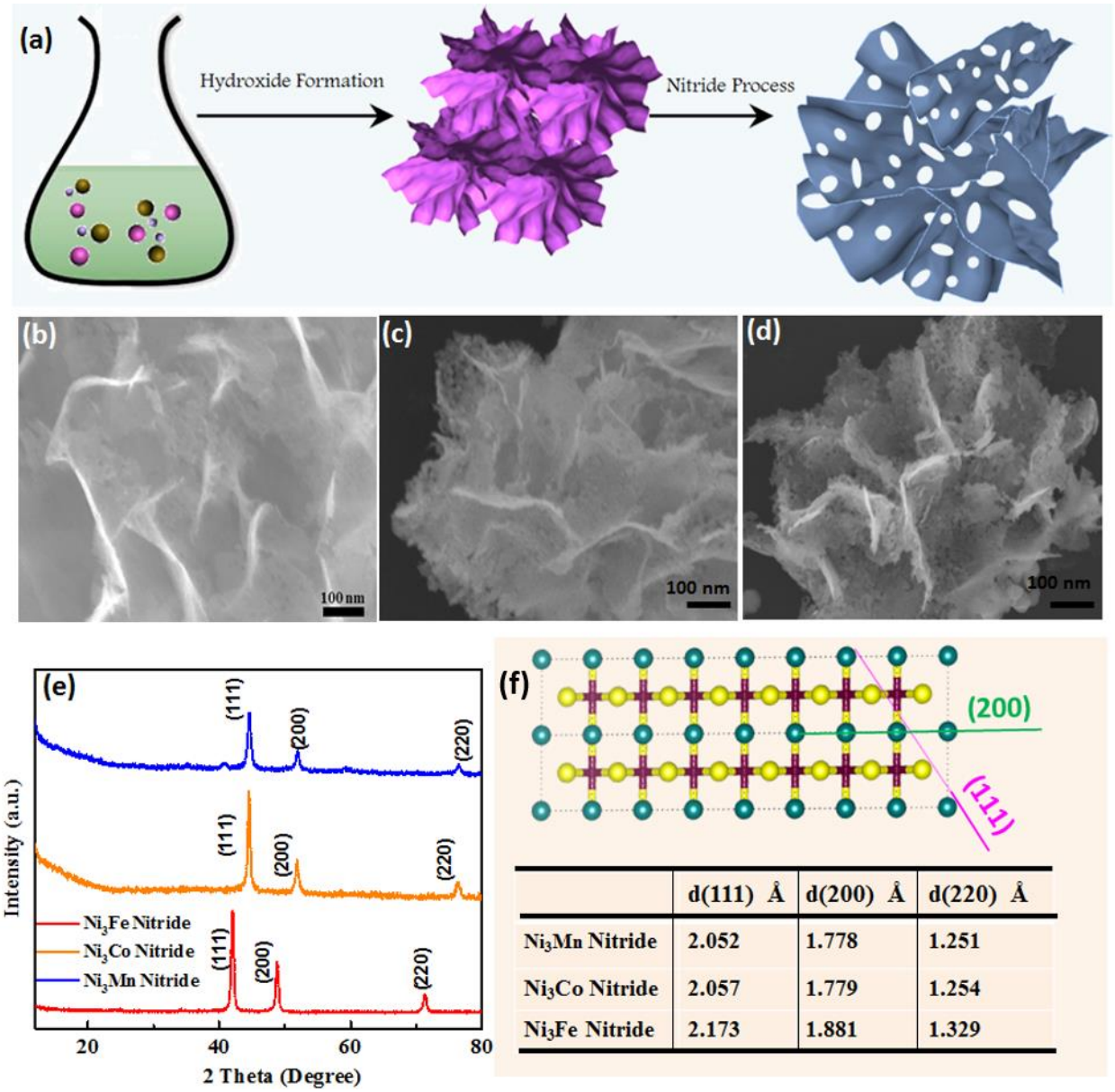

	d(111) Å	d(200) Å	d(220) Å
Ni_3Mn Nitride	2.052	1.778	1.251
Ni_3Co Nitride	2.057	1.779	1.254
Ni_3Fe Nitride	2.173	1.881	1.329

Figure 1. (a) Fabrication process of 2D holey Ni_3M nitride; SEM images of (b) 2D holey Ni_3Fe nitride; (c) 2D holey Ni_3Co nitride; (d) 2D holey Ni_3Mn nitride; (e) XRD pattern and (f) the corresponding distance of lattice plate.

The variations of the surface area and pore size range before and after nitridation process were further characterized, as shown in **Figure 2**. Taking Ni_3Fe nitride for example, after the nitridation process, the specific surface area was dramatically enlarged from 114.9 to 189.6 m^2 g^{-1}, while numerous nanopores were generated, with the process primarily driven by the phase

transformation and Kirkendall effect. [13-14, 50] Meanwhile, the specific surface area of Ni_3Co nitride, and Ni_3Mn nitride were dramatically increased from 125.6 to 197.2, and from 108.5 to 168.3m^2 g^{-1}, respectively. Compared to those deposited on porous substrate, such as nickel foam, a remarkable enhancement of specific surface area was got because the high weight ratio of the substrate will decrease the whole electrode specific surface area to some extent. [51-52] It is concluded that designed ultrathin holey 2D structured nitrides can be successfully obtained by annealing the corresponding LDH precursors, and the surface area can be dramatically increased by the generation of numerous holes on the large lateral surface.

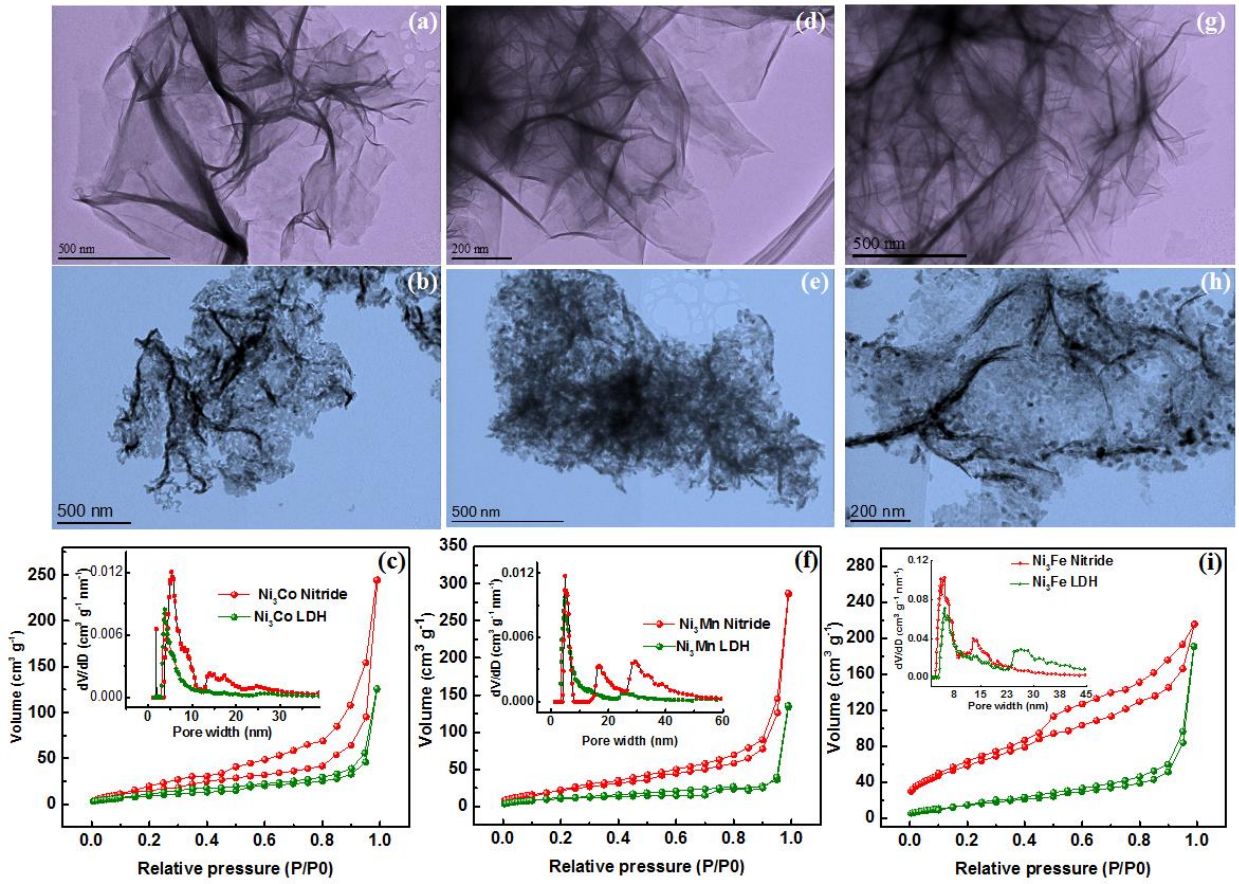

Figure 2. TEM images of 2D holey Ni_3M (M = Co, Mn, Fe) LDH nanosheets; 2D holey Ni_3M (M = Co, Mn, Fe) nitride nanosheets and Specific surface area of 2D Ni_3M (M = Co, Mn, Fe) LDH nanosheets and 2D holey Ni_3M nitride nanosheets (c); inset: pore size distributions; (a - c) M = Co; (d - f) M = Mn; (g - i) M = Fe.

Morphological characterization of the as-fabricated materials was studied by scanning TEM energy-dispersive X-ray spectroscopy (STEM-EDS) and atomic force microscopy (AFM), as shown in **Figure 3** and **Figures S3-4**. Compatible with the conclusions on the surface area and pore distribution, nitride materials present an obvious holey structure with pore size ~ 15 nm. Meanwhile, all the elements demonstrate a homogenous distribution over the whole area and maintain similar molar ratios (**Figure S5** and **Table S1)**. Furthermore, after the nitridation process, a solo phase component distribution still exists, which is compatible with the XRD. The AFM was employed to estimate the thickness and surface structure of the as-synthesized 2D holey Ni_3Fe nitride nanosheets. As revealed in Figure 3g-j, the thickness of 2D holey Ni_3Fe nitride nanosheets is within the range of 0.6-0.8 nm, a thickness of approximately 3 atomic layers of (001) lattice planes. The trend in the curves also indicates the holey structure on the lateral 2D surfaces. High-angle annular dark-field STEM (HAADF-STEM) was utilized to characterize the structure of the ultrathin nitride nanosheets. As indicated in Figure 3k, l and **Figures S6-7**, in contrast to the intact surfaces, these holey nanosheets generate numerous edge areas and expose abundant lattice plates, which can thereby provide abundant catalytically active sites. More importantly, the ultrathin nanosheets show a nearly single-crystal structure with a strong high-orientation pattern, which can significantly increase the electrical conductivity. It is well acknowledged that there is a definite link between electrical conductivity and catalytic activity. High electrical conductivity can dramatically accelerate the kinetic rate of the catalytic reaction. [39, 44, 53] Generally, the integration of the huge surface area, abundant defects the exposed catalytic sites near the edges, and the ultrahigh electrical conductivity resulting from the nearly single-crystal structure, as well as the connected holey architecture will make this type of nitride nanosheet a satisfactory electrocatalyst, particularly for gas generation processes.

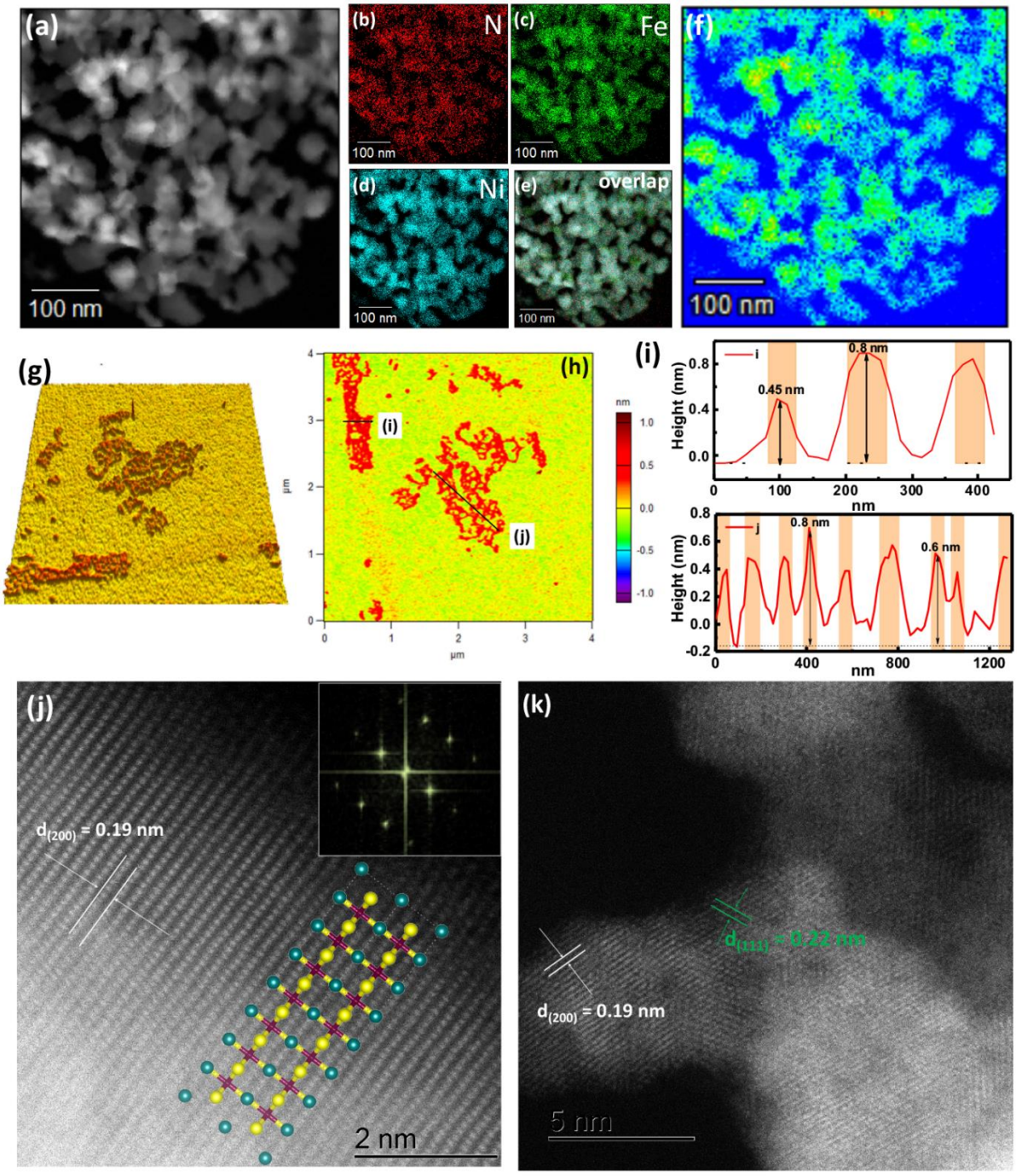

Figure 3. (a) HAADF-STEM image of holey Ni_3Fe nitride nanosheets; (b-e) STEM-EDS mapping of (a); (f) the phase distribution in (a); (g-j) AFM results for the holey Ni_3Fe nitride nanosheets; (k, l) HAADF-STEM images of holey Ni_3Fe nitride nanosheets; molecular diagram with fast Fourier transform (FFT) pattern as inset image in (k).

A rotating disk electrode (RDE) was utilized to explore the electrocatalytic properties of these 2D structured materials, including LDH and holey nitride nanosheets, commercial IrO_2 and Pt/C with 1.0 M KOH. IrO_2 was purchased from Sigma with the size about 100 nm, as shown in **Figure S8**. The OER curves were investigated to determine each sample's OER catalytic activity based on mass-normalized current density (**Figure 4a** and **Figure S9-12**). It is obvious that the 2D holey Ni_3Fe nitride nanosheets exhibit the highest current density compared with Ni_3Co nitride, Ni_3Mn nitride, and IrO_2. A quite small overpotential (300 mV) is required for the 2D holey Ni_3Fe nitride nanosheets to deliver the current density about 100 A g^{-1}, which is smaller than those of 2D holey Ni_3Co nitride nanosheets (340 mV), 2D holey Ni_3Mn nitride nanosheets (429 mV), and IrO_2 (465 mV). The small peak at 1.46 V of the Ni_3Fe nitride could be ascribed to the redox reaction of $Ni^{2+}/Ni^{3+}/Ni^{4+}$.[54] The 2D nickel-based LDH and 2D nickel-based oxides nanosheets were also investigated for comparison (**Figure S9 and Figure S10**). To generate 100 A g^{-1}, 2D Ni_3Fe LDH nanosheets, 2D Ni_3Co LDH nanosheets, and 2D Ni_3Mn LDH nanosheets required the overpotential of 413, 430, and 423 mV, respectively. Meanwhile, 2D Ni_3Fe oxide nanosheets, 2D Ni_3Co oxide nanosheets, and 2D Ni_3Mn oxide nanosheets required the overpotential of 357, 369, and 386 mV, respectively. It is clear that those 2D Ni_3M LDH nanosheet composites have higher overpotentials than their corresponding holey 2D nickel-based nitride nanosheet counterparts, which can be attributed to the excellent electrical conductivity, the architecture, and the numerous highly catalytically active sites. As revealed in Figure 4b, c, the excellent OER activities of the 2D holey Ni_3Fe nitride nanosheets were further confirmed by using Tafel plots and overpotential. The 2D porous Ni_3Fe nitride nanosheets has the smallest Tafel slope (51 mV dec^{-1}), indicating more enhanced OER kinetic activity for the holey 2D Ni_3Fe nitride electrode when comparing with Ni_3Co nitride (55 mV dec^{-1}), Ni_3Mn nitride (64 mV dec^{-1}), and IrO_2 (69 mV dec^{-1}). As revealed in

Figure 4d, the holey 2D Ni_3M nitride nanosheets exhibit huge activity enhancements over the commercial IrO_2, which could be due to excellent conductivity of the Ni_3M nitrides and the holey nanosheets structure. In particular, the holey 2D Ni_3Fe nitride nanosheets reveals the highest performance compared with IrO_2. With overpotential of 300 mV, the 2D porous Ni_3Fe nitride nanosheet sample shows an improvement over IrO_2 by a factor of nearly 25 times. Moreover, we investigated the long-term electrocatalytic stability of these 2D holey Ni_3M nitride nanosheets with high current density (100 A g^{-1}), as revealed in Figure 4e. Obviously, the holey 2D Ni_3Fe nitride nanosheet electrode requires the lowest overpotential compared to the holey 2D Ni_3Co nitride nanosheets and holey 2D Ni_3Mn nitride nanosheets, indicating its excellent stability and electrocatalytic activity. For comparison, Ni_3Fe nitride nanoparticles with the size about 20 nm were also synthesized (**Figure S11)**. As shown in **Figure S12a**, the Ni_3Fe nitride nanoparticles also demonstrate a good OER performance, with a small overpotential (303 mV). However, the stability of the Ni_3Fe nitride nanoparticles is quite low compared with the 2D holey Ni_3Fe nitride nanosheets. As demonstrated in **Figure S12b**, the Ni_3Fe nitride nanoparticles has significant performance decay, which could be contributed to the aggregation of the small nanoparticles. The excellent OER activities of the holey 2D Ni_3Fe nitride nanosheets could be ascribed to its excellent electrical conductivity and the numerous catalytically active sites provided by the newly formed in-plane nanopores. Moreover, the metallic nitride products exhibit excellent electrical conductivity (Figure 4f, **Figure S13**, and **Table S2)**, resulting from their metallic properties, highly-orientated crystalline texture, and large lattice spacing, which is also superior to those of reported nitride and other types of materials, such as sulfides, oxides and phosphates, primarily resulting from the highly orientated crystal structure. [28, 32, 39] The electrical conductivity were further measured by four-probe method. The electrical conductivity of Ni_3Fe nitride is 270 S m^{-1},

which is higher than that of Ni_3Co nitride (200 S m^{-1}) and Ni_3Mn nitride (70 S m^{-1}). In addition, the highest conductivity of Ni_3Fe nitride could be attributed to its larger crystal lattice, which could significantly facilitate the electron transport and leading to excellent conductivity.

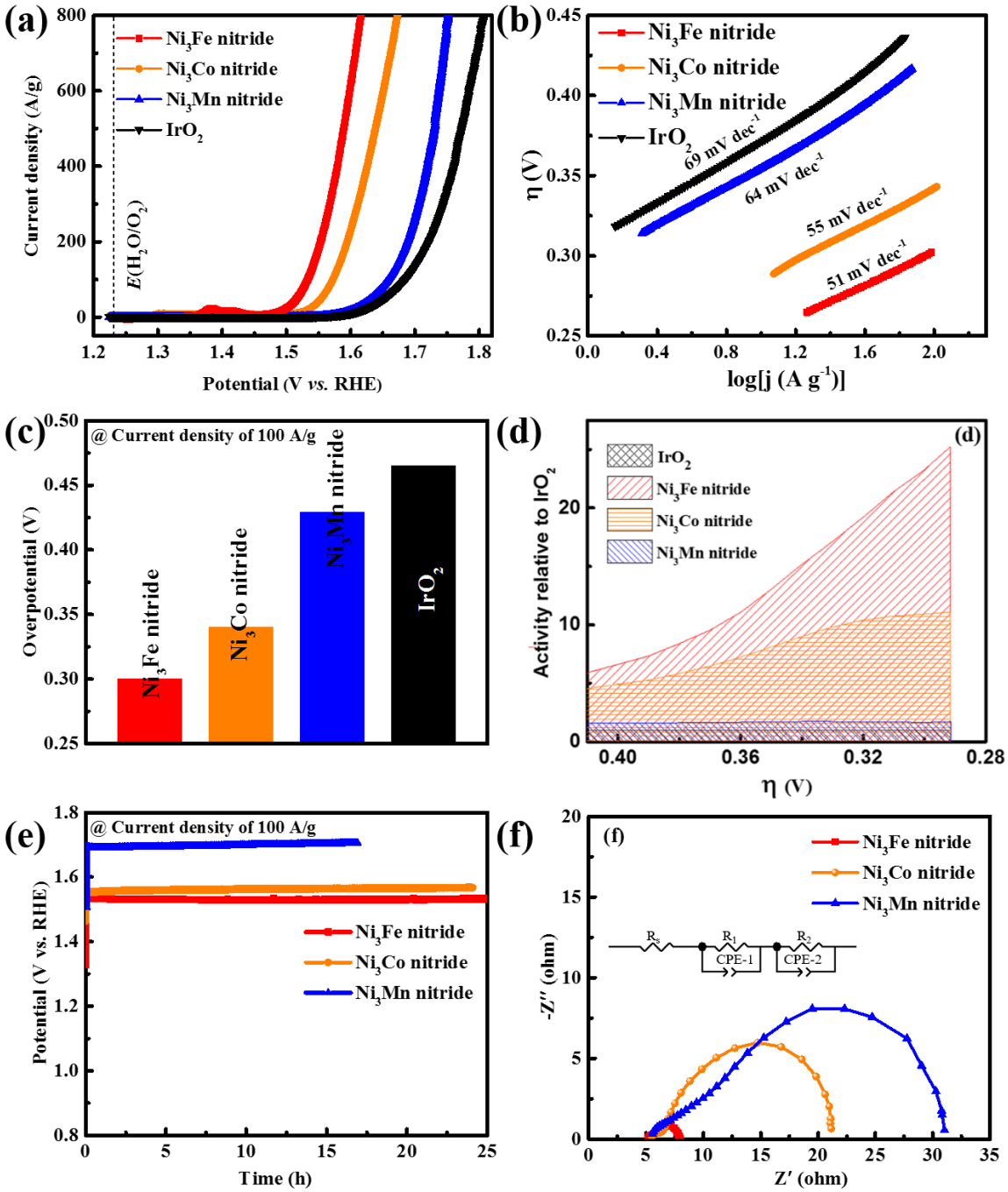

Figure 4. (a) Linear sweep voltammetrys (LSVs) of 2D holey Ni_3M Nitride nanosheets and IrO_2 with for the OER based on mass-normalized current density (scan rate of 10 mV s^{-1}); (b) Tafel plots of 2D holey Ni_3M Nitride nanosheets and IrO_2; (c) The overpotential required to realize the current density of 100 A g^{-1}; (d) Corresponding activity enhancement of 2D holey Ni_3M Nitride nanosheets relative to IrO_2; (e) Stability curves of the 2D porous Ni_3M nitride nanosheets; (f) Electrochemical impedance spectroscopy (EIS) curves of holey Ni_3M nitride nanosheets, the equivalent circuit diagram as inset. RHE: reversible hydrogen electrode.

In addition, the electrocatalytic HER activities of these holey 2D Ni_3M nitride nanosheets were also studied in 1.0 M KOH (Ar-saturated). The holey 2D Ni_3Fe nitride nanosheets electrode exhibited a quite tiny onset potential (209 mV), which is just huger than Pt/C (50 mV), but it is obviously smaller than those of the holey 2D Ni_3Co nitride nanosheets (273 mV) and the holey 2D Ni_3Mn nitride nanosheets (282 mV) (**Figure 5a-e)**. Also, the holey 2D Ni_3Fe nitride nanosheets exhibited a small overpotential (233 mV) to realize the current density about -100 A g^{-1}, which is only bigger than Pt/C (95 mV) but smaller than the holey 2D Ni_3Co nitride nanosheets (319 mV) and the holey 2D Ni_3Mn nitride nanosheets (451 mV). Moreover, the HER current density of the holey 2D Ni_3Fe nitride nanosheets is considerable higher than those of the holey 2D Ni_3Co nitride nanosheets and the holey 2D Ni_3Mn nitride nanosheets at a given voltage. For instance, the current density of the 2D holey Ni_3Fe nitride nanosheets is -492.4 A g^{-1} with overpotential about 300 mV. This is 6.54 and 12.54 times higher than those of the holey 2D Ni_3Co nitride nanosheets and the holey 2D Ni_3Mn nitride nanosheets, respectively. Meanwhile, the holey 2D Ni_3Fe nitride nanosheets demonstrated an enhanced reaction kinetic rate with a lower Tafel slope than for the commercial Pt/C. After 1000 cycles, there is no obvious passivation of catalytic activity, as shown in **Figure 5(f)**. On basis of the above results, it is clear that the holey 2D nickel-based nitrides nanosheets derived from 2D nickel-based LDH nanosheets have significantly enhanced OER and HER catalytic activities. The improved catalytic activities can be due to the excellent conductivity

of the Ni_3M nitrides, abundant active sites, and huge surface area provided by the 2D holey nanosheet structure. It is clear that the 2D holey Ni_3Fe nitride nanosheets with holey nanostructure exhibit a lower overpotential used as OER and HER bifunctional electrocatalyst.

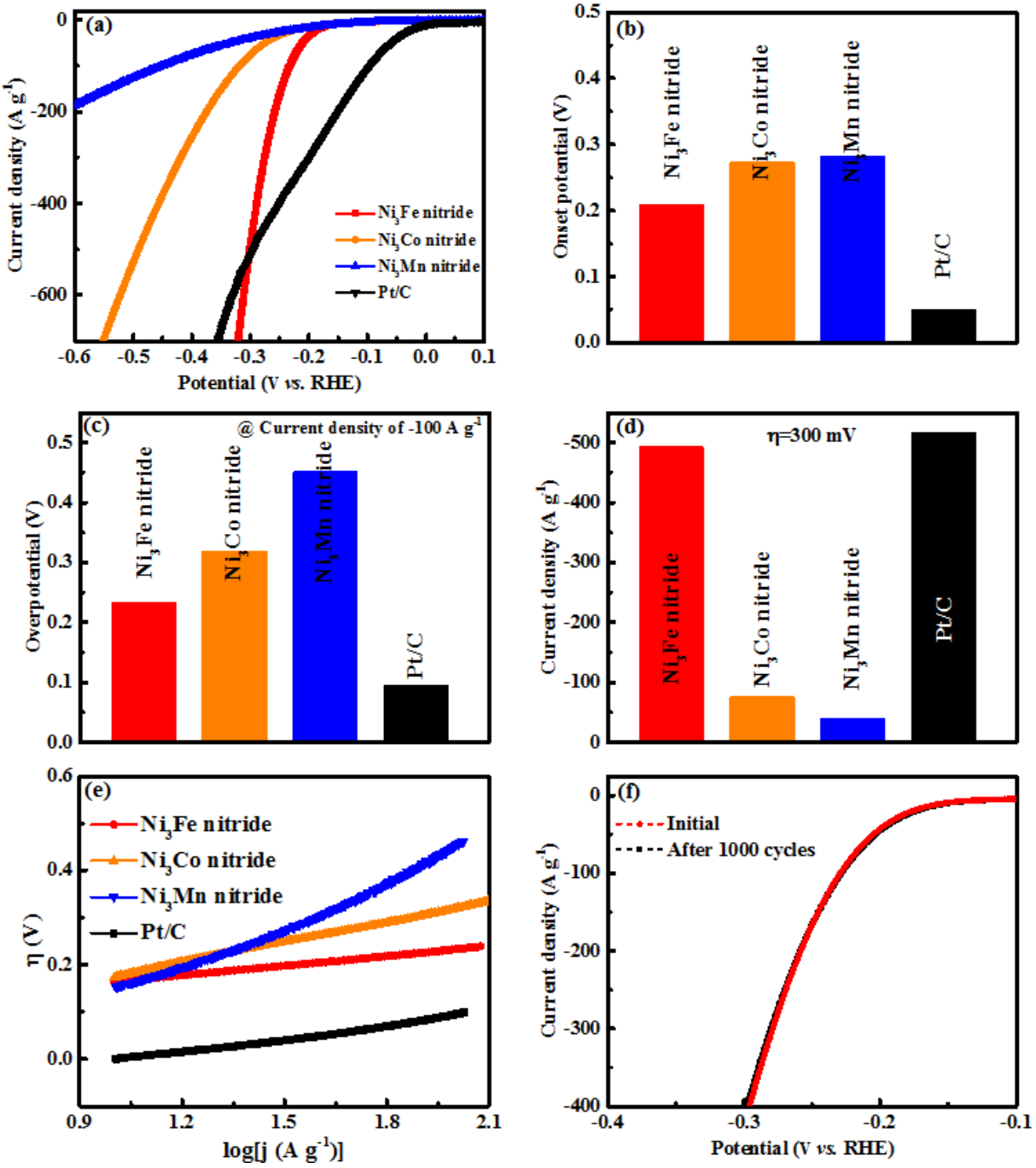

Figure 5. (a) LSVs of 2D holey Ni_3M nitride nanosheets and Pt/C for the HER based on mass-normalized current density (scan rate of 10 mV s^{-1}); (b) Comparison of the onset potentials; (c)

The overpotential required for achieve the current density of 100 A g^{-1}; (d) Current density at η = -300 mV; (e) The corresponding Tafel plots for 2D holey Ni_3M nitride nanosheets and Pt/C; (f) LSV curves of holey 2D Ni_3Fe nitride nanosheets before and after 1000 cycles.

It is well known that there is a definite link between catalytic performance and active surface area, therefore, the electrochemical surface area (ECSA) was calculated through the corresponding electrochemical double-layer capacitance (C_{dl}) to demonstrate the advantages of the 2D holey nanosheets structure in determining the catalytic activity. [55-58] The slope of capacitive current density ($\Delta j = j_{anode} - j_{cathode}$) at 1.273 V against different scan rates is twice of the C_{dl}, utilized to stand for the corresponding ECSA. Typical CV curves of Ni_3Fe nitride, Ni_3Co nitride, Ni_3Mn nitride, and nickel-based LDH in different scan rates are shown in **Figure 6(a - c)** and **Figure S14**. As can be seen in **Figure 6(d)**, 2D holey Ni_3Fe nitride exhibits the largest C_{dl} compared with those of the other catalysts. From LDH to 2D holey nitride, the ECSA values increased by around twice. This increase is mainly assigned to the formation of abundant defects and uniform nanopores on the nanosheets during the nitridation process. More importantly, compared with 2D holey Ni_3Co nitride and Ni_3Mn nitride nanosheets, 2D holey Ni_3Fe nitride nanosheets has 104.2 % and 128.8 % higher ECSA, more than 9 - fold and 64 - fold times of OER current density at η = 320 mV achieved, respectively. Such enhancement of the electrocatalytic activity can not only be ascribed to the larger surface area, but also due to the higher intrinsic catalytic activity due to the significantly enlarged lattice spacing after introducing nitrogen, leading to much more electrochemically accessible inner layer surface.

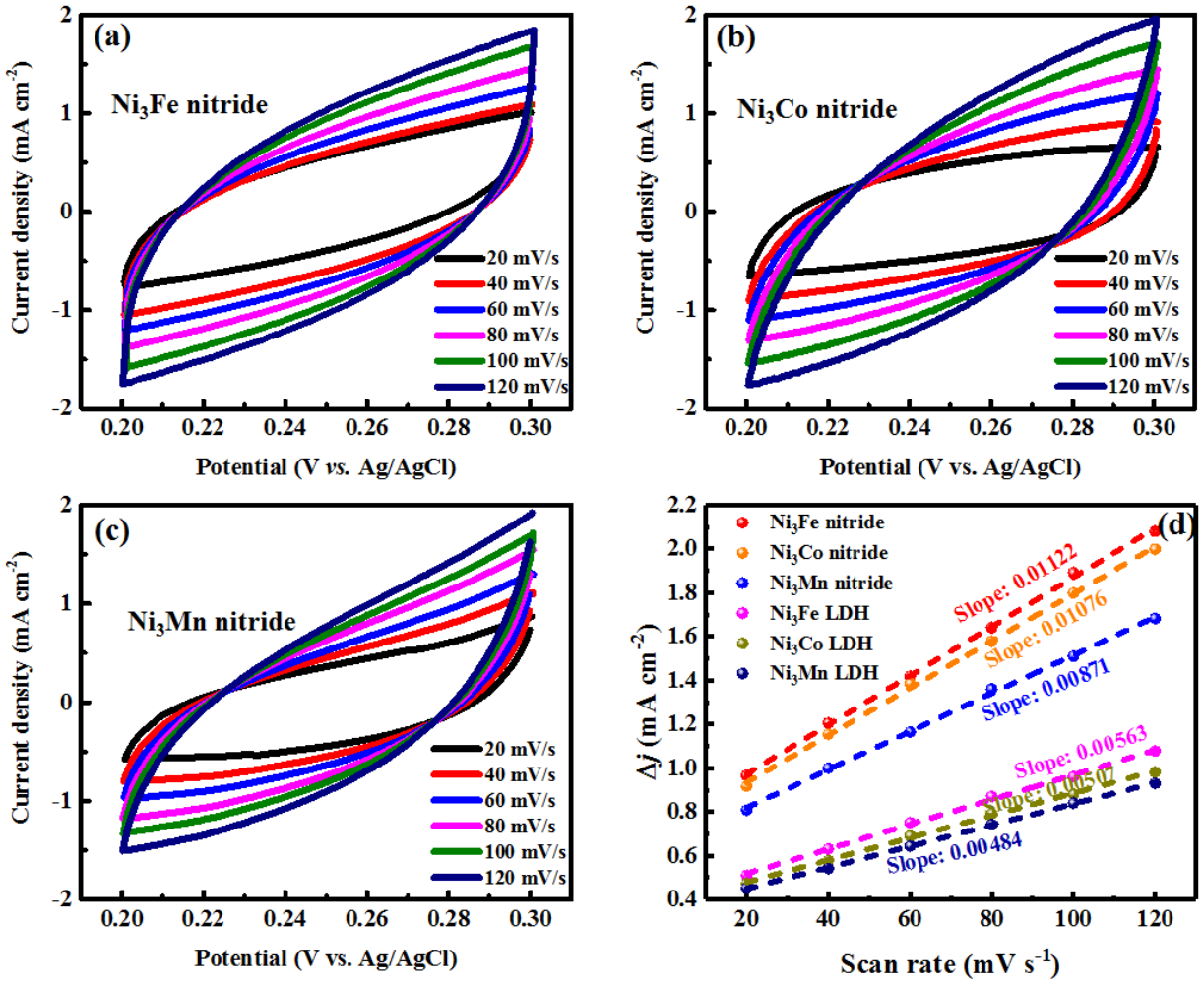

Figure 6. Typical CV curves of (a) Ni_3Fe nitride, (b) Ni_3Co nitride, and (c) Ni_3Mn nitride in 1M KOH with various scan rates. (d) Differences of current density ($\Delta j = j_{anode} - j_{cathode}$) at 1.273 V plotted vs. the scan rates. The C_{dl} is half of the slope.

The overall water-splitting performance of 2D holey Ni_3Fe nitride nanosheets was evaluated in 1.0 M KOH, in which Ni_3Fe nitride was utilized as electrocatalyst both at the two electrodes. The electrocatalyst achieved a current density about 100 A g^{-1} at 1.60 V (**Figure S15a**). The inset in Figure S15a reveals the formation of oxygen and hydrogen bubbles on the nickel foam. The electrolyser exhibits considerable overall water-splitting durability for over 10 h with no obvious performance decay (Figure S15b). The Faradaic efficiency of this electrolyser was determined with chronopotentiometry over 120 min (inset in Figure S15b). The inset in Figure S15b

demonstrated that the H_2 generated experimentally were similar with the theoretically calculated results during this time. The overall water-splitting has a very high Faradaic efficiency (close to 100 %). These results also suggest that the 2D holey Ni_3Fe nitride nanosheets are promising bifunctional electrocatalysts for economically efficient water-splitting electrocatalysts.

Even after 1000 CV cycles, the Ni_3Fe nitride nanosheets still preserve the 2D holey morphology (**Figure S16a)**. HRTEM image indicates that there is a quite thin oxides layer about 1-2 nm on the Ni_3Fe nitride nanosheets (Figure S16b), suggesting the oxidization of Ni_3Fe nitride nanosheets. The compositions changes of the 2D holey Ni_3Fe nitride nanosheets after 1000 CV cycles were explored with X-ray photoelectron spectroscopy (XPS), as revealed in Figure S16d - f. The peaks of Ni^{2+} and Fe^{3+} indicate that the existence of surface oxidation in Ni_3Fe nitride nanosheets into NiFe oxide/hydroxide. However, there is no NiFe oxide/hydroxide diffraction peak, indicating the main phase was still Ni_3Fe nitride (Figure S16c). In addition, there is no significant elements contents changes before and after CV cycles (**Table S3**). All of the above characterizations provide solid evidence that the major phases are Ni_3Fe nitride with a very thin oxide layer during the catalytic process.

To further investigate and understand the enhanced OER and HER performance of the Ni_3Fe nitride, the oxygen adsorption energy (E_O) and hydrogen adsorption energy (E_H) on the Ni_3Fe nitride (111) and (200) lattice were studied by conducting density functional theory (DFT) calculations. **Figure S17a-d** and **Table S4** reveal that the (111) lattice possesses more moderate hydrogen adsorption energy (-1.18 eV) and oxygen adsorption energy (-3.47 eV) than these of the (200) lattice (-3.87 and -6.93 eV, respectively), indicating that the (111) lattice is more favorable

than the (200) lattice for the OER and HER reactions. DFT calculations for the E_O and E_H on the Ni_3Fe nitride (111), Ni_3Co nitride (111), and Ni_3Mn nitride (111) were further conducted. **Figure S17c-h** and **Table S4** demonstrate that the Ni_3Fe nitride (111) possesses a moderate oxygen adsorption energy (-3.47 eV), which is favorable for the OER reaction than that of Ni_3Co nitride (111) (-2.80 eV) and Ni_3Mn nitride (111) (-3.29 eV). In addition, Ni_3Fe nitride (111) also exhibits optimized hydrogen adsorption energy (-1.18eV) when compared with Ni_3Co nitride (111) (-0.67 eV) and Ni_3Mn nitride (111) (-0.59 eV). The above calculations could prove that the larger lattice spacing could enhance the catalytic activities through changing the hydrogen adsorption energy and oxygen adsorption energy.

4. CONCLUSIONS

In summary, ultrathin holey 2D nickel-based nitride lateral nanosheets (less than 1 nm thick) were designed and successfully synthesized by nitridation treatment of the corresponding hydroxide precursors. Owing to the highly-orientated crystalline texture, large lattice spacing, abundant exposed catalytically active sites resulting both from the atoms on the large lateral surfaces and the areas near the edges of the generated holes, as well as the hierarchical porous continuously conductive architecture suitable for transport of intermediate reaction products and diffusion of generated gases, these metallic nitride holey nanosheets showed excellent electrocatalytic property for the OER and HER. Among them, the ultrathin holey 2D Ni_3Fe nitride nanosheets demonstrated a quite lower overpotential (300 mV) towards oxygen evolution to deliver a current density of 100 A g^{-1}, a large enhancement over commercial IrO_2 by a factor of nearly 25 times. Meanwhile, they also accelerate the catalytic HER with a tiny overpotential (233

mV) to achieve the current density about 100 A g^{-1}, a kinetic rate higher than commercial Pt/C catalytic activity. The robust electrocatalytic activity of 2D Ni_3Fe nitride nanosheets is largely ascribed to the enhanced electrochemical surface area, owing to the larger surface area and excellent intrinsic electrocatalytic property due to the significantly enlarged lattice spacing after introducing nitrogen, leading to much more electrochemically accessible inner layer surface. Therefore, in this work, the concept of designing 2D ultrathin highly-orientated and holey nitride nanosheets has been explored for electrocatalyst application.

ASSOCIATED CONTENT

Supporting Information

The Supporting Information is available free of charge on the ACS Publications website.

Additional STEM, EDS, OER, and EIS (PDF)

AUTHOR INFORMATION

Corresponding Authors

*E-mail for W.B. Luo: luow@uow.edu.au

*E-mail for J.Z. Wang: jiazhao@uow.edu.au

Notes

The authors declare no competing financial interest.

ACKNOWLEDGEMENTS

This work is financially supported by the Australian Research Council (ARC) through a Discovery Project (DP140100401) and ARC-LIEF Grants (LE120100104 and LE0237478).The authors appreciate Dr. Tania Silver to polish the manuscript with English editing, and also thank the UOW Electron Microscopy Centre for the use of the equipment, with specific acknowledgements to Dr. Gilberto Casillas-Garcia. All the authors have discussed and approved the final revised version of the manuscript.

REFERENCES

1. Bhimanapati, G. R.; Lin, Z.; Meunier, V.; Jung, Y.; Cha, J.; Das, S.; Xiao, D.; Son, Y.; Strano, M. S.; Cooper, V. R.; Liang, L.; Louie, S. G.; Ringe, E.; Zhou, W.; Kim, S. S.; Naik, R. R.; Sumpter, B. G.; Terrones, H.; Xia, F.; Wang, Y.; Zhu, J.; Akinwande, D.; Alem, N.; Schuller, J. A.; Schaak, R. E.; Terrones, M.; Robinson, J. A., Recent Advances in Two-Dimensional Materials beyond Graphene. *ACS Nano* **2015,** *9*, 11509-11539.
2. Tan, C.; Cao, X.; Wu, X.-J.; He, Q.; Yang, J.; Zhang, X.; Chen, J.; Zhao, W.; Han, S.; Nam, G.-H.; Sindoro, M.; Zhang, H., Recent Advances in Ultrathin Two-Dimensional Nanomaterials. *Chem. Rev.* **2017,** *117*, 6225-6331.
3. Chhowalla, M.; Liu, Z.; Zhang, H., Two-dimensional transition metal dichalcogenide (TMD) nanosheets. *Chem. Soc. Rev.* **2015,** *44*, 2584-2586.
4. Dou, Y.; Zhang, L.; Xu, X.; Sun, Z.; Liao, T.; Dou, S. X., Atomically thin non-layered nanomaterials for energy storage and conversion. *Chem. Soc. Rev.* **2017,** *46*, 7338-7373.
5. Khan, A. H.; Ghosh, S.; Pradhan, B.; Dalui, A.; Shrestha, L. K.; Acharya, S.; Ariga, K., Two-Dimensional (2D) Nanomaterials towards Electrochemical Nanoarchitectonics in Energy-Related Applications. *Bull. Chem. Soc. Jpn.* **2017,** *90*, 627-648.
6. Chen, P.; Zhang, Z.; Duan, X.; Duan, X., Chemical synthesis of two-dimensional atomic crystals, heterostructures and superlattices. *Chem. Soc. Rev.* **2018,** *47*, 3129-3151.
7. Butler, S. Z.; Hollen, S. M.; Cao, L.; Cui, Y.; Gupta, J. A.; Gutiérrez, H. R.; Heinz, T. F.; Hong, S. S.; Huang, J.; Ismach, A. F.; Johnston-Halperin, E.; Kuno, M.; Plashnitsa, V. V.; Robinson, R. D.; Ruoff, R. S.; Salahuddin, S.; Shan, J.; Shi, L.; Spencer, M. G.; Terrones, M.; Windl, W.; Goldberger, J. E., Progress, Challenges, and Opportunities in Two-Dimensional Materials Beyond Graphene. *ACS Nano* **2013,** *7*, 2898-2926.
8. Zhang, H., Ultrathin Two-Dimensional Nanomaterials. *ACS Nano* **2015,** *9*, 9451-9469.
9. Shi, Y.; Li, H.; Li, L.-J., Recent advances in controlled synthesis of two-dimensional transition metal dichalcogenides via vapour deposition techniques. *Chem. Soc. Rev.* **2015,** *44*, 2744-2756.

10. Tan, C.; Zhang, H., Two-dimensional transition metal dichalcogenide nanosheet-based composites. *Chem. Soc. Rev.* **2015,** *44*, 2713-2731.
11. Auxilia, F. M.; Ishihara, S.; Mandal, S.; Tanabe, T.; Saravanan, G.; Ramesh, G. V.; Umezawa, N.; Hara, T.; Ya Xu, Y.; Hishita, S.; Yamauchi, Y.; Dakshanamoorthy, A.; Hill, J. P.; Ariga, K.; Abe, H. Low-Temperature Remediation of NO Catalyzed by Interleaved CuO Nanoplates. Adv. Mater. 2014, 26, 4481-4485.
12. Wang, K.; Wei, M.; Morris, M. A.; Zhou, H.; Holmes, J. D., Mesoporous Titania Nanotubes: Their Preparation and Application as Electrode Materials for Rechargeable Lithium Batteries. *Adv. Mater.* **2007,** *19*, 3016-3020.
13. Xia, X.; Wang, Y.; Ruditskiy, A.; Xia, Y., 25th Anniversary Article: Galvanic Replacement: A Simple and Versatile Route to Hollow Nanostructures with Tunable and Well-Controlled Properties. *Adv. Mater.* **2013,** *25*, 6313-6333.
14. Luo, W.-B.; Gao, X.-W.; Chou, S.-L.; Wang, J.-Z.; Liu, H.-K., Porous AgPd–Pd Composite Nanotubes as Highly Efficient Electrocatalysts for Lithium–Oxygen Batteries. *Adv. Mater.* **2015,** *27*, 6862-6869.
15. Feng, J. X.; Xu, H.; Dong, Y. T.; Ye, S. H.; Tong, Y. X.; Li, G. R., FeOOH/Co/FeOOH Hybrid Nanotube Arrays as High-Performance Electrocatalysts for the Oxygen Evolution Reaction. *Angew. Chem., Int. Ed.* **2016,** *55*, 3694-3698.
16. Feng, J. X.; Ye, S. H.; Xu, H.; Tong, Y. X.; Li, G. R., Design and Synthesis of FeOOH/CeO2 Heterolayered Nanotube Electrocatalysts for the Oxygen Evolution Reaction. *Adv Mater* **2016,** *28*, 4698-4703.
17. Lu, X. F.; Gu, L. F.; Wang, J. W.; Wu, J. X.; Liao, P. Q.; Li, G. R., Bimetal-Organic Framework Derived CoFe2 O4 /C Porous Hybrid Nanorod Arrays as High-Performance Electrocatalysts for Oxygen Evolution Reaction. *Adv Mater* **2017,** *29*, 1604437.
18. Ye, S. H.; Shi, Z. X.; Feng, J. X.; Tong, Y. X.; Li, G. R., Activating CoOOH Porous Nanosheet Arrays by Partial Iron Substitution for Efficient Oxygen Evolution Reaction. *Angew. Chem., Int. Ed.* **2018,** *57*, 2672-2676.
19. Sun, Y.; Gao, S.; Lei, F.; Xie, Y., Atomically-thin two-dimensional sheets for understanding active sites in catalysis. *Chem. Soc. Rev.* **2015,** *44*, 623-636.
20. Chen, D.; Peng, L.; Yuan, Y.; Zhu, Y.; Fang, Z.; Yan, C.; Chen, G.; Shahbazian-Yassar, R.; Lu, J.; Amine, K.; Yu, G., Two-Dimensional Holey Co3O4 Nanosheets for High-Rate Alkali-Ion Batteries: From Rational Synthesis to in Situ Probing. *Nano Lett.* **2017,** *17*, 3907-3913.
21. Duan, X.; Wang, C.; Pan, A.; Yu, R.; Duan, X., Two-dimensional transition metal dichalcogenides as atomically thin semiconductors: opportunities and challenges. *Chem. Soc. Rev.* **2015,** *44*, 8859-8876.
22. Luo, W.-B.; Gao, X.-W.; Shi, D.-Q.; Chou, S.-L.; Wang, J.-Z.; Liu, H.-K., Binder-Free and Carbon-Free 3D Porous Air Electrode for Li-O2 Batteries with High Efficiency, High Capacity, and Long Life. *Small* **2016,** *12*, 3031-3038.
23. Wang, P.; Pu, Z.; Li, Y.; Wu, L.; Tu, Z.; Jiang, M.; Kou, Z.; Amiinu, I. S.; Mu, S., Iron-Doped Nickel Phosphide Nanosheet Arrays: An Efficient Bifunctional Electrocatalyst for Water Splitting. *ACS Appl. Mater. Interfaces* **2017,** *9*, 26001-26007.
24. Pu, Z.; Amiinu, I. S.; Zhang, C.; Wang, M.; Kou, Z.; Mu, S., Phytic acid-derivative transition metal phosphides encapsulated in N,P-codoped carbon: an efficient and durable hydrogen evolution electrocatalyst in a wide pH range. *Nanoscale* **2017,** *9*, 3555-3560.

25. Pu, Z. H.; Xue, Y.; Li, W. Q.; Amiinu, I. S.; Mu, S. C., Efficient water splitting catalyzed by flexible NiP2 nanosheet array electrodes under both neutral and alkaline solutions. *New J. Chem.* **2017,** *41*, 2154-2159.
26. Pu, Z.; Zhang, C.; Amiinu, I. S.; Li, W.; Wu, L.; Mu, S., General Strategy for the Synthesis of Transition-Metal Phosphide/N-Doped Carbon Frameworks for Hydrogen and Oxygen Evolution. *ACS Appl. Mater. Interfaces* **2017,** *9*, 16187-16193.
27. Chen, P.; Zhou, T.; Xing, L.; Xu, K.; Tong, Y.; Xie, H.; Zhang, L.; Yan, W.; Chu, W.; Wu, C.; Xie, Y., Atomically Dispersed Iron–Nitrogen Species as Electrocatalysts for Bifunctional Oxygen Evolution and Reduction Reactions. *Angew. Chem., Int. Ed.* **2017,** *56*, 610-614.
28. Konkena, B.; Masa, J.; Botz, A. J. R.; Sinev, I.; Xia, W.; Koßmann, J.; Drautz, R.; Muhler, M.; Schuhmann, W., Metallic NiPS3@NiOOH Core–Shell Heterostructures as Highly Efficient and Stable Electrocatalyst for the Oxygen Evolution Reaction. *ACS Catal.* **2017,** *7*, 229-237.
29. Luo, W.-B.; Chou, S.-L.; Wang, J.-Z.; Zhai, Y.-C.; Liu, H.-K., A Metal-Free, Free-Standing, Macroporous Graphene@g-C3N4 Composite Air Electrode for High-Energy Lithium Oxygen Batteries. *Small* **2015,** *11*, 2817-2824.
30. Xu, K.; Ding, H.; Lv, H.; Tao, S.; Chen, P.; Wu, X.; Chu, W.; Wu, C.; Xie, Y., Understanding Structure-Dependent Catalytic Performance of Nickel Selenides for Electrochemical Water Oxidation. *ACS Catal.* **2017,** *7*, 310-315.
31. Chen, G.-F.; Ma, T. Y.; Liu, Z.-Q.; Li, N.; Su, Y.-Z.; Davey, K.; Qiao, S.-Z., Efficient and Stable Bifunctional Electrocatalysts Ni/NixMy (M = P, S) for Overall Water Splitting. *Adv. Funct. Mater.* **2016,** *26*, 3314-3323.
32. Yu, F.; Zhou, H.; Zhu, Z.; Sun, J.; He, R.; Bao, J.; Chen, S.; Ren, Z., Three-Dimensional Nanoporous Iron Nitride Film as an Efficient Electrocatalyst for Water Oxidation. *ACS Catal.* **2017,** *7*, 2052-2057.
33. Zhang, B.; Xiao, C.; Xie, S.; Liang, J.; Chen, X.; Tang, Y., Iron–Nickel Nitride Nanostructures in Situ Grown on Surface-Redox-Etching Nickel Foam: Efficient and Ultrasustainable Electrocatalysts for Overall Water Splitting. *Chem. Mater.* **2016,** *28*, 6934-6941.
34. Yu, J.; Li, Q.; Li, Y.; Xu, C.-Y.; Zhen, L.; Dravid, V. P.; Wu, J., Ternary Metal Phosphide with Triple-Layered Structure as a Low-Cost and Efficient Electrocatalyst for Bifunctional Water Splitting. *Adv. Funct. Mater.* **2016,** *26*, 7644-7651.
35. Chen, J. G.; Jones, C. W.; Linic, S.; Stamenkovic, V. R., Best Practices in Pursuit of Topics in Heterogeneous Electrocatalysis. *ACS Catal.* **2017,** *7*, 6392-6393.
36. Lopes, P. P.; Strmcnik, D.; Tripkovic, D.; Connell, J. G.; Stamenkovic, V.; Markovic, N. M., Relationships between Atomic Level Surface Structure and Stability/Activity of Platinum Surface Atoms in Aqueous Environments. *ACS Catal.* **2016,** *6*, 2536-2544.
37. Yang, L.; Lv, Y. L.; Cao, D. P., Co,N-codoped nanotube/graphene 1D/2D heterostructure for efficient oxygen reduction and hydrogen evolution reactions. *J. Mater. Chem. A* **2018,** *6*, 3926-3932.
38. Gao, M. Y.; Zeng, J. R.; Zhang, Q. B.; Yang, C.; Li, X. T.; Hua, Y. X.; Xu, C. Y., Scalable one-step electrochemical deposition of nanoporous amorphous S-doped NiFe2O4/Ni3Fe composite films as highly efficient electrocatalysts for oxygen evolution with ultrahigh stability. *J. Mater. Chem. A* **2018,** *6*, 1551-1560.
39. Xu, K.; Chen, P.; Li, X.; Tong, Y.; Ding, H.; Wu, X.; Chu, W.; Peng, Z.; Wu, C.; Xie, Y., Metallic Nickel Nitride Nanosheets Realizing Enhanced Electrochemical Water Oxidation. *J. Am. Chem. Soc.* **2015,** *137*, 4119-4125.

40. Li, S. W.; Wang, Y. C.; Peng, S. J.; Zhang, L. J.; Al-Enizi, A. M.; Zhang, H.; Sun, X. H.; Zheng, G. F., Co-Ni-Based Nanotubes/Nanosheets as Efficient Water Splitting Electrocatalysts. *Adv. Energy Mater.* **2016,** *6*, 1501661.
41. Yang, Y.; Fei, H.; Ruan, G.; Li, Y.; Tour, J. M., Vertically Aligned WS_2 Nanosheets for Water Splitting. *Adv. Funct. Mater.* **2015,** *25*, 6199-6204.
42. Gao, D. Q.; Zhang, J. Y.; Wang, T. T.; Xiao, W.; Tao, K.; Xue, D. S.; Ding, J., Metallic Ni3N nanosheets with exposed active surface sites for efficient hydrogen evolution. *J. Mater. Chem. A* **2016,** *4*, 17363-17369.
43. Jin, S., Are Metal Chalcogenides, Nitrides, and Phosphides Oxygen Evolution Catalysts or Bifunctional Catalysts? *ACS Energy Lett.* **2017,** *2*, 1937-1938.
44. Long, X.; Li, G.; Wang, Z.; Zhu, H.; Zhang, T.; Xiao, S.; Guo, W.; Yang, S., Metallic Iron–Nickel Sulfide Ultrathin Nanosheets As a Highly Active Electrocatalyst for Hydrogen Evolution Reaction in Acidic Media. *J. Am. Chem. Soc.* **2015,** *137*, 11900-11903.
45. Li, R.; Hu, Z.; Shao, X.; Cheng, P.; Li, S.; Yu, W.; Lin, W.; Yuan, D., Large Scale Synthesis of NiCo Layered Double Hydroxides for Superior Asymmetric Electrochemical Capacitor. *Sci. Rep.* **2016,** *6*, 18737.
46. Song, F.; Hu, X., Ultrathin Cobalt–Manganese Layered Double Hydroxide Is an Efficient Oxygen Evolution Catalyst. *J. Am. Chem. Soc.* **2014,** *136*, 16481-16484.
47. Lopes, P. P.; Tripkovic, D.; Martins, P. F. B. D.; Strmcnik, D.; Ticianelli, E. A.; Stamenkovic, V. R.; Markovic, N. M., Dynamics of electrochemical Pt dissolution at atomic and molecular levels. *J. Electroanal. Chem.* **2018,** *819*, 123-129.
48. Wang, H.; Xu, S.; Tsai, C.; Li, Y.; Liu, C.; Zhao, J.; Liu, Y.; Yuan, H.; Abild-Pedersen, F.; Prinz, F. B.; Nørskov, J. K.; Cui, Y., Direct and continuous strain control of catalysts with tunable battery electrode materials. *Science* **2016,** *354*, 1031-1036.
49. Luo, M. C.; Guo, S. J., Strain-controlled electrocatalysis on multimetallic nanomaterials. *Nat. Rev. Mater.* **2017,** *2*, 17059.
50. Zhang, D.; Sun, W.; Zhang, Y.; Dou, Y.; Jiang, Y.; Dou, S. X., Engineering Hierarchical Hollow Nickel Sulfide Spheres for High-Performance Sodium Storage. *Adv. Funct. Mater.* **2016,** *26*, 7479-7485.
51. Pham, T. V.; Guo, H. P.; Luo, W. B.; Chou, S. L.; Wang, J. Z.; Liu, H. K., Carbon- and binder-free 3D porous perovskite oxide air electrode for rechargeable lithium-oxygen batteries. *J. Mater. Chem. A* **2017,** *5*, 5283-5289.
52. Liu, W.-M.; Gao, T.-T.; Yang, Y.; Sun, Q.; Fu, Z.-W., A hierarchical three-dimensional NiCo2O4 nanowire array/carbon cloth as an air electrode for nonaqueous Li-air batteries. *Phys. Chem. Chem. Phys.* **2013,** *15*, 15806-15810.
53. Luo, W.-B.; Pham, T. V.; Guo, H.-P.; Liu, H.-K.; Dou, S.-X., Three-Dimensional Array of TiN@Pt_3Cu Nanowires as an Efficient Porous Electrode for the Lithium–Oxygen Battery. *ACS Nano* **2017,** *11*, 1747-1754.
54. Gong, M.; Li, Y.; Wang, H.; Liang, Y.; Wu, J. Z.; Zhou, J.; Wang, J.; Regier, T.; Wei, F.; Dai, H., An Advanced Ni–Fe Layered Double Hydroxide Electrocatalyst for Water Oxidation. *J. Am. Chem. Soc.* **2013,** *135*, 8452-8455.
55. Song, F.; Hu, X., Exfoliation of layered double hydroxides for enhanced oxygen evolution catalysis. *Nat Commun* **2014,** *5*, 4477.
56. Dou, Y.; Zhang, L.; Xu, J.; He, C. T.; Xu, X.; Sun, Z.; Liao, T.; Nagy, B.; Liu, P.; Dou, S. X., Manipulating the Architecture of Atomically Thin Transition Metal (Hydr)oxides for Enhanced Oxygen Evolution Catalysis. *ACS Nano* **2018,** *12*, 1878-1886.

57. McCrory, C. C. L.; Jung, S.; Peters, J. C.; Jaramillo, T. F., Benchmarking Heterogeneous Electrocatalysts for the Oxygen Evolution Reaction. *J. Am. Chem. Soc.* **2013,** *135*, 16977-16987.
58. Konkena, B.; Puring, K. J.; Sinev, I.; Piontek, S.; Khavryuchenko, O.; Durholt, J. P.; Schmid, R.; Tuysuz, H.; Muhler, M.; Schuhmann, W.; Apfel, U. P., Pentlandite rocks as sustainable and stable efficient electrocatalysts for hydrogen generation. *Nat. Commun.* **2016,** *7*, 12269.

TOC: